10328–10342 *Nucleic Acids Research, 2022, Vol. 50, No. 18* *Published online 21 September 2022*
https://doi.org/10.1093/nar/gkac757

Chromatin transitions triggered by LH density as epigenetic regulators of the genome

Stephanie Portillo-Ledesma[1], Meghna Wagley[1] and Tamar Schlick[1,2,3,4,*]

[1]Department of Chemistry, New York University, 1001 Silver, 100 Washington Square East, New York, NY 10003, USA, [2]New York University-East China Normal University Center for Computational Chemistry at New York University Shanghai, Room 340, Geography Building, 3663 North Zhongshan Road, Shanghai 200062, China, [3]Courant Institute of Mathematical Sciences, New York University, 251 Mercer St, New York, NY 10012, USA and [4]Simons Center for Computational Physical Chemistry, 24 Waverly Place, Silver Building, New York University, New York, NY 10003 USA

Received May 31, 2022; Revised July 26, 2022; Editorial Decision August 19, 2022; Accepted September 02, 2022

ABSTRACT

Motivated by experiments connecting linker histone (LH) deficiency to lymphoma progression and retinal disorders, we study by mesoscale chromatin modeling how LH density (ρ) induces gradual, as well sudden, changes in chromatin architecture and how the process depends on DNA linker length, LH binding dynamics and binding mode, salt concentration, tail modifications, and combinations of ρ and linker DNA length. We show that ρ tightly regulates the overall shape and compaction of the fiber, triggering a transition from an irregular disordered state to a compact and ordered structure. Such a structural transition, resembling B to A compartment transition connected with lymphoma of B cells, appears to occur around $\rho = 0.5$. The associated mechanism is DNA stem formation by LH binding, which is optimal when the lengths of the DNA linker and LH C-terminal domain are similar. Chromatin internal and external parameters are key regulators, promoting or impeding the transition. The LH density thus emerges as a critical tunable variable in controlling cellular functions through structural transitions of the genome.

INTRODUCTION

While the hierarchical chromatin organization in the cell nucleus is not well understood, recent technological advances are helping shed light on genome architecture, changing our view of chromatin from a static and ordered structure to a highly dynamic and heterogeneous polymer (1,2).

Overall, DNA wraps around the eight histone core proteins to form the nucleosome, and an extended chain of nucleosomes connected by linker DNA establishes the 10 nm chromatin fiber at low salt with a predominant zigzag secondary structure (3). As the fiber folds at physiological salt, nucleosomes form groups or 'clutches' of different sizes and compaction (4–7). Such chromatin fibers then establish topologically associating domains (TADs) (8) by loop extrusion (9). Further organization and separation of active genes from silenced genes leads to the formation of compartments (10). Finally, chromosomes occupy specific territories directed by interactions among them and with the nuclear lamina (11).

The auxiliary protein linker histone (LH) has emerged as a key factor in chromatin architecture and genome integrity. LH binds to the nucleosome at the dyad axis to further compact chromatin into 30 nm fibers (12) through a DNA 'stem' formation mechanism in which the entering and exiting linker DNAs are brought into close juxtaposition for 3–5 nm before diverging (12). Its density (ρ) within the fiber, defined as the number of LHs per nucleosome, can vary from 0.03 to 1.3 (13). Yet, LH function extends beyond chromatin compaction, as these proteins are subject to multiple post translational modifications and have many interacting partners, influencing DNA transcription, replication and repair, and controlling the epigenetic landscape of the genome (14,15).

The binding of LH to the nucleosome is also dynamic; LHs exchange continuously with the pool of unbound LH (16,17). At least three populations have been detected: a freely diffusing population; a weakly bound population with residence times on the scale of seconds; and a more stably bound population with residence times on the scale of minutes, present mostly in heterochromatin (16,17). Such binding dynamics are affected by several factors, including phosphorylation, which increases the exchange due to a 20% reduction in affinity (17–19); acetylation, which accelerates exchange (17,20); mutations in the globular domain, which reduce binding affinity and accelerate exchange (21); and LH variants, where some variants have a tight association and thus slow binding dynamics (22) compared to others that exchange more rapidly (23). In two previous studies, we simulated chromatin fibers with dynamic LH binding and determined that fast and slow binding

*To whom correspondence should be addressed. Tel: +1 212 998 3116; Email: schlick@nyu.edu

act cooperatively to control fiber unfolding (24) and that dynamic binding reduces fiber stiffness compared to fixed LH (25).

Mammals express 11 LH variants (26). Experiments in mouse have shown that deletion of only one variant (H1c, H1d, or H1e) does not disrupt development due to compensation by other subtypes (27,28). However, deletion of three subtypes (H1c, H1e and H1d) results in 50% reduced LH levels, which inhibits embryonic stem cell differentiation (29) and can be lethal (30). Similarly, deletion of H1c, H1e and H1(0) triggers heterochromatin decompaction in mouse rod photoreceptors, affecting retina maturation (31). LH depletion has also been related to cancer development. Specifically, recurrent LH mutations have been observed in 30–50% of large B cell, Hodgkin and follicular lymphomas (32–34) but associated mechanisms are not known. In a recent study, we showed how LH depletion leads to lymphoma of B cells (35) and found that cells with mutant LHs exhibit chromatin architectural changes, characterized by a shift of chromatin from the silenced compartment B to the active compartment A. Our modeling of chromatin fibers with decreasing ρ showed that chromatin fibers transition from a compact/straight to a relaxed/globular state, resembling the B to A transition. This transition is also consistent with the recent report that increasing ρ may promote chromatin phase separation (36).

In a prior work, we showed how LH modulates chromatin higher order folding (37). Fibers typical of metaphase, depleted of LH, exhibit hierarchical looping folding, which involves the looping of loosely folded zigzag arrays, whereas fibers typical of interphase, with high ρ, appear more compact and form well-defined 30 nm zigzag fibers. Similarly, chromatin modeling by other groups showed that LH depletion increases fiber flexibility (38), decreases fiber extension (38), and facilitates loops formation on the Kb scale (39).

Here, we explore the role of ρ in chromatin architecture and transitions in relation to LH depletion associated to lymphoma of B-cells and retinal disorders. In particular, we seek to pinpoint how changes in ρ trigger chromatin structural transitions, whether these are smooth or sudden transitions, where a critical density can be determined, and how they depend on other internal and external variables, like linker DNA length/pattern, LH binding dynamics and binding mode, histone tails, salt concentration, and LH phosphorylation.

Overall, our results suggest that a value around $\rho = 0.5$ induces a structural transition of chromatin fibers with medium length linker DNAs by forming rigid nucleosome DNA stems. This transition can be promoted or impeded by salt concentrations and post translational modifications. Thus, ρ acts as an epigenetic regulator that tightly controls chromatin compaction and shape. A specific transition density such as 0.5 can be a key element in the repression or activation of specific genes, and in this way can affect disease propensity and progression. In particular, human diseases such as retinal disorders (40) or lymphoma (35) likely progress depending on the excess or deficiency of LH levels. Our findings thus suggest ways to influence these processes through the amount of LH.

MATERIALS AND METHODS

Chromatin model

We use our nucleosome resolution mesoscale model to study 100-nucleosome chromatin fibers with different ρ.

Chromatin elements are coarse grained from the atomistic structures at different levels of resolution (Supplementary Figure S1). The nucleosome core particle with wrapped DNA is coarse grained from the nucleosome core crystal structure as a 300-charged points cylinder (41). Charges are calculated with our discrete surface charge optimization (DiSCO) algorithm (42,43) that assigns charges on the irregular surface determined by the Debye–Hückel potential. Flexible histone tails, coarse grained as five residues per bead, are added to the nucleosome core particle based on Brownian dynamics simulations (44). Such modeling is applied to N-terminal tails of H2A, H2B, H3, and H4 and the C-terminal tail of H2A (44). The charge on each bead is the net sum of the charges of the five residues that constitute the bead. Connecting nucleosomes is the linker DNA, modeled with a combined wormlike chain and bead model that has a resolution of ≈9 bp (45). Each DNA bead has a negative charge calculated with the Stigter procedure at a specific salt concentration (46). LHs H1E (based on the rat H1.4) and H1C (based on the mouse H1.2), bound to the entry/exit sites of the nucleosome, are coarse grained similarly as 5 residues per bead with each bead's charge determined by DiSCO (47,48). We resolve the globular and the C-terminal domain (CTD), while neglecting the N-terminal domain, which is believed less important for chromatin compaction (49). The main difference between our H1E and H1C coarse grained models is the presence of one more bead in the C-terminal domain of H1E (22 versus 21 beads in H1C). Both LHs can bind to the nucleosome symmetrically (on-dyad) or in two off-dyad modes in which the LH is rotated $+20^{o}$ or -20^{o} around the axis perpendicular to the nucleosome plane, passing through the nucleosome center (48). We develop a phosphorylated version of LHs by changing the total charge of the CTD beads containing Ser/Thr residues. The charge is modified by considering a negative charge on those residues of -1.68e instead of 0, similar to what we did in (50). This produces a reduction in the CTD charge of 22e for H1E (≈40%) and 13e for H1C (≈20%) (Supplementary Table S1). Magnesium ions are modeled implicitly (3) with a phenomenological approach that modifies the DNA–DNA repulsion energy term by increasing the inverse of the Debye length from 1.52 to 2.5 nm^{-1} so linker DNAs can be closer, and decreasing the DNA persistence length from 50 to 30 nm, based on experimental data showing increased DNA flexibility at 1 mM divalent ions (51,52).

Energy terms in the model include bending, stretching, and twisting for the linker DNA and histone tails, stretching and bending for the LHs, Debye–Hückel terms for the electrostatic interaction between beads, and excluded volume terms for all beads treated with the Lennard-Jones potential (47,53).

Chromatin fibers are simulated using a tailored Monte Carlo (MC) algorithm that efficiently samples the conformational states of oligonucleosomes (54). Seven MC moves are used for sampling. The global pivot move (with prob-

ability 0.1) randomly selects linker DNA beads or nucleosome cores and then rotates the shorter part of the oligonucleosome by an angle between 0 and 20° about a randomly selected axis that passes through the element. Local translation and rotation moves (both with probabilities 0.05) randomly select a linker DNA bead or nucleosome core and translate the bead between 0 and 0.6 nm or rotate the bead by an angle between 0 and 36° around a randomly selected axis. The global pivot and local rotation and translation moves are accepted or rejected based on the standard Metropolis criterion (55). Histone tails are sampled using a configurational bias MC method (with probability 0.70) (44). In this method, a histone chain is randomly selected and regrown bead-by-bead with the Rosenbluth scheme (56). LHs are sampled with local translational moves (with probability 0.098), applied only to the C-terminal domain (47) which are also accepted based on the Metropolis criterion (55). To enhance the sampling of the oligonucleosome configurations, we further employ an end-transfer move in which a randomly selected terminal portion of the oligonucleosome fiber is transferred from one end to the other and regrown with the Rosenbluth scheme (56). The seventh MC move is related to the attaching/detaching of LHs to nucleosomes (with probability 0.002), as presented below.

Linker histone dynamic binding

Based on the initial development of LH dynamic binding in our chromatin mesoscale model (24,25), we updated our current simulation code to consider LH dynamic binding using an 'stop-and-go' approach. Specifically, we include an additional Monte Carlo move that allows LHs to bind and unbind to the nucleosome cores during the simulation based on the specific combination of $\{P_{bind},\ P_{unb}\}$ probabilities, where both P_{bind} and P_{unb} are between 0 and 1.

The algorithm works as follows:

1) The simulation starts with LHs bound to every nucleosome.
2) In a random Monte Carlo step a core is selected.
3) If the core has an LH bound, an attempt is made to unbind it with probability P_{unb}.
4) If the core has no LH bound, an attempt is made to bind it with probability P_{bind}.
5) The bound LH configuration is accepted or rejected based on the Metropolis criterion by generating a random number $r \in (0, 1)$ and accepting the new state if $P < r$, being P:

$$P = min\{1,\ \exp[-\beta\,(U_{new} - U_{old})]\}, \qquad (1)$$

where $\beta = 1/K_BT$ and U_{new} and U_{old} the energies of the new and old configurations.

P_{unb} and P_{bind} define the dissociation and association probabilities and determine the fraction of LHs bound to the chromatin fiber, or equivalently ρ, in each Monte Carlo step as follows:

$$\text{fraction of bound LHs} = \frac{P_{bind}}{P_{bind} + P_{unb}} \qquad (2)$$

Thus, each $\{P_{bind},\ P_{unb}\}$ pair mimics an average effective ρ across the simulation where each fiber in the equilibrium ensemble has around the same number of LHs bound, but these are located in different nucleosomes.

To implement unbinding, we eliminate all LH interactions with other chromatin elements, such as nucleosome cores, linker DNA, histone tails, and other LHs. Effectively, we count all interaction energy terms involving LH as zero. To avoid clashes between the LHs and other chromatin elements upon binding, we introduce an additional LH relaxation step. Namely, a Monte Carlo procedure of 500 steps is used to move randomly selected LH beads by translational displacements, while accounting for the full interactions and corresponding energy between LHs and other chromatin elements. Thus, upon LH binding, LH beads are usually in reasonable positions, but if not (energies are high due to clashes), we reject the binding according to the Metropolis criterion.

Fiber systems

We study at different ρ fibers in which we vary the following parameters (Table 1): (i) DNA linker length, using 26, 35, 44, 53, 62, 70 and 80 bp, and a non-uniform linker DNA distribution; (ii) dynamic versus static LH binding; (iii) on versus off–dyad LH binding mode; (iv) wildtype versus truncated tails; (v) wildtype versus phosphorylated LH and (vi) physiological versus low and high salt concentration.

Our non-uniform fiber model follows the linker DNA distribution obtained by Voong et al. in mouse embryonic stem cells (57). As shown in Supplementary Figure S2, we partition the frequency plot obtained by Voong *et al.* in seven regions representing the seven linker DNAs our model can handle due to coarse graining (58): 26–80 bp (2–8 beads). We then calculate the area of each region by numerical integration to find the percentage of each linker DNA, obtaining: 30% 26 bp; 17% 35 bp; 15% 44 bp; 13% 53 bp; 9% 62 bp; 7% 71 bp; and 9% 80 bp. Finally, the fiber system is set up so that these linker DNAs are randomly distributed along the fiber. Namely, using a random function that returns a uniform variate from 0 to 1, each linker DNA is assigned a random number. Then, the linker length value is assigned based on the ranking of that linker length as shown in Supplementary Table S2.

For all systems, we use a 50/50 H1E/H1C distribution of this pair of variants for each ρ studied because, in nature, their ratios (59) and their binding affinities (60) are similar.

Simulation details and analysis

All simulations are conducted at a temperature of 293 K and a monovalent salt (NaCl) concentration of 150 mM, unless otherwise specified. For each system, we run 10 independent MC simulations starting from a different random seed generator number and a randomly chosen DNA twist value of 0, 12 or –12° to mimic natural variations (61). The initial configurations are in an ideal zigzag conformation as we have shown zigzag to be the dominant configuration under physiological conditions (3). Simulations are performed for 50 million MC steps and the last 10 million steps of each trajectory are used for analysis, producing ensembles of 1000 configurations. Structural properties are determined for these 1000 structures, and averages and standard deviations are calculated. Convergence is monitored

Table 1. Simulations studied in this work. Fiber systems are described by a combination of parameters: linker DNA, LH binding dynamics, LH binding mode, wildtype/truncated tail state, wildtype/phosphorylated LH state and salt condition

	Simulation condition					
System linker DNA (bp)	Dynamic (D) vs. static (S) LH	On vs. off-dyad LH	WT vs. truncated (T) tails	WT vs. phosphorylated (P) LH	NaCl (mM)	Trajectory label[a]
26	D	On	WT	WT	150	26_D
	S	On	WT	WT	150	26_S
35	D	On	WT	WT	150	35_D
	S	On	WT	WT	150	35_S
44	D	On	WT	WT	150	44_D
	S	On	WT	WT	150	44_S
	S	Off +20	WT	WT	150	44_S_+20
	S	Off –20	WT	WT	150	44_S_-20
	S	On	T	WT	150	44_S_T
	S	On	WT	P	150	44_S_P
	S	On	WT	WT	15	44_S_L
	S	On	WT	WT	150 + Mg^{2+}	44_S_H
53	D	On	WT	WT	150	53_D
	S	On	WT	WT	150	53_S
62	D	On	WT	WT	150	62_D
	S	On	WT	WT	150	62_S
70	D	On	WT	WT	150	70_D
	S	On	WT	WT	150	70_S
	S	Off +20	WT	WT	150	70_S_+20
	S	Off –20	WT	WT	150	70_S_-20
	S	On	T	WT	150	70_S_T
	S	On	WT	P	150	70_S_P
	S	On	WT	WT	15	70_S_L
	S	On	WT	WT	150 + Mg^{2+}	70_S_H
80	D	On	WT	WT	150	80_D
	S	On	WT	WT	150	80_S
Non-uniform	D	On	WT	WT	150	nu_D
	S	On	WT	WT	150	nu_S
	S	Off +20	WT	WT	150	nu_S_+20
	S	Off –20	WT	WT	150	nu_S_-20
	S	On	T	WT	150	nu_S_T
	S	On	WT	P	150	nu_S_P
	S	On	WT	WT	15	nu_S_L
	S	On	WT	WT	150 + Mg^{2+}	nu_S_H

[a]By default, we consider on-dyad binding, wildtype tails, wildtype LH and 150 mM NaCl. Thus, we denote in the trajectory label when the simulation conditions deviate from these.

by analyzing global and local properties across the simulations to ensure equilibration, which usually occurs well within 20–30 million MC steps. See Supplementary Figure S3 for convergence of energy, packing ratio and sedimentation coefficient.

Chromatin packing ratio. The number of nucleosomes present in 11 nm of fiber is calculated as follows:

$$Packing\,ratio = \frac{11 * N_C}{Fiber\,length}, \quad (3)$$

where N_C is the number of nucleosomes in the fiber. To measure the fiber length in each chromatin configuration, we compute the length of the fiber axis passing through the nucleosome cores (Supplementary Figure S4). The fiber axis is defined as a three-dimensional parametric curve as follows:

$$\boldsymbol{r}^{ax}(i) = \left(r_1^{ax}(i), r_2^{ax}(i), r_3^{ax}(i)\right), \quad (4)$$

where $r_1^{ax}(i)$, $r_2^{ax}(i)$, and $r_3^{ax}(i)$ are piecewise polynomials created by performing a cubic smoothing spline interpolation (with smoothing parameter of 0.35) to the nucleosomes x, y and z coordinates. The polynomials are evaluated at each nucleosome to obtain their center position in the x, y and z directions. Then, we calculate the Euclidean distance between every nucleosome i and $i + 2$ across the fiber as the difference between the vectors defined by the center position in the x, y and z directions. At the end, all Euclidean distances are summed to obtain the total fiber length.

Nucleosome dimer distance, triplet angle, and DNA entry/exit angle. Local distances between consecutive nucleosomes are calculated for each pair of nucleosomes $\{i, i + 1\}$. Triplet angles for three consecutive nucleosomes refer to the angle defined by the center of nucleosomes i, $i + 1$, and $i + 2$. DNA entry/exit angle in a nucleosome is determined by the directions of the entry and exit linker DNAs, which are defined by the vector connecting the first and second DNA beads in each linker DNA. These properties are calculated for each configuration and then probability distributions are determined for the 1000–configuration ensemble.

Internucleosome interactions. Two nucleosomes are assumed to be in contact if the distance between any element (core or histone tails) is <1.8 nm. Nucleosome contact frequencies are calculated for the combined trajectory that

contains 1000 configurations, 100 configurations from each of the 10 individual trajectories. The frequencies are then normalized by the total number of configurations. Contact matrices are further decomposed into one-dimensional plots that depict the magnitude of i, $i \pm k$ interactions as follows:

$$I(k) = \frac{\sum_{i=1}^{N_C} I'(i, i \pm k)}{\sum_{j=1}^{N_C} I(j)}, \quad (5)$$

where I' is the contact matrix and N_C the total number of cores.

Tail interactions. For each chromatin configuration, we calculate the interactions between each tail t and other chromatin element e, such as linker DNA, nucleosome cores, or other tails. For linker DNA and nucleosome cores, we distinguish between parental (the element belongs to the same nucleosome as the tail) and non-parental (the element belongs to a different nucleosome from the tail) interactions. Whereas the interactions with other tails are calculated only with non-parental tails.

Thus, we construct a two-dimensional matrix, where each matrix element T' is defined as:

$$T'_{(t,e)} = \text{mean}\left[\frac{1}{N_C N_e}\sum_{i\in I_C}\sum_{j_e=1}^{N_e}\delta_{i,j_e}^{t,e}(M)\right], \quad (6)$$

where

$$\delta_{i,j_e}^{t,e}(M) = \begin{cases} 1 \text{ if contact} \\ 0 \text{ otherwise} \end{cases}$$

N_c is the total number of nucleosomes, N_e is the number of chromatin elements, I_c is a specific nucleosome along the chromatin fiber, and M is a specific chromatin configuration. Thus $\delta_{i,j_e}^{t,e}(M) = 1$ if j_e is an e-type element 'in contact' with a t-type tail of nucleosome i at configuration M.

The interactions are counted when the distance between the beads of two interacting elements is less than 1.8 nm and every tail is considered to be either interacting with only one element or free. In the case of the interactions with the nucleosome core, we measure the distance between the histone tail beads and the 300-point charges of the nucleosome core.

Interaction frequencies are then normalized as follows:

$$T_{(t,e)} \underline{\text{def}} \frac{T'_{(t,e)}}{\sum_{e'=1}^{N_e} T'_{(t,e')}} \quad (7)$$

Linker histone interactions. Similarly, we determine the interactions between the CTD of the LH and parental and non-parental DNA. The two elements are considered in contact when the distance between them is less than half the sum of their van der Waals radii, 2.7 nm. Interaction frequencies are calculated from the combined trajectory that contains 1000 configurations.

Nucleosome projections. We analyze the linker DNA positional distribution by determining the position vector of each DNA bead, $\mathbf{d}_{ij}$, in the frame of reference of the parental nucleosome core with center of mass position r_i and orientation $\{\mathbf{a}_i, \mathbf{b}_i, \mathbf{c}_i\}$. The projected distribution is then denoted by $\mathbf{d}_{ij} = \{\mathbf{d}'_{ij,x}, \mathbf{d}'_{ij,y}, \mathbf{d}'_{ij,z}\}$, where $\mathbf{d}'_{ij,x} = \mathbf{a_i} \cdot (\mathbf{d}_{ij} - \boldsymbol{r}_i)$, $\mathbf{d}'_{ij,y} = \mathbf{b_i} \cdot (\mathbf{d}_{ij} - \boldsymbol{r}_i)$, and $\mathbf{d}'_{ij,z} = \mathbf{c_i} \cdot (\mathbf{d}_{ij} - \boldsymbol{r}_i)$. The three-dimensional distribution is viewed in two dimensions along the nucleosomal plane given by $(\mathbf{d}'_{ij,x}, \mathbf{d}'_{ij,y})$. Thus, figures of nucleosome projections display a characteristic chromatosome snapshot as well as the cumulative (red) and average (blue) positions of the linker DNA in the nucleosome top view along with the LH globular head position (yellow) and average CTD position (cyan).

Table 2. P_{bind} and P_{unb} parameters, effective average ρ from Equation (2), and associated scenario

P_{bind}	P_{unb}	Effective average ρ	Scenario
0	1	0	No binding
0.25	1	0.20 ± 0.05	Very low affinity; very slow binding
0.75	1	0.44 ± 0.06	Low affinity; slow binding
0.5	0.5	0.49 ± 0.06	Moderate affinity; intermediate binding
1	0.75	0.56 ± 0.07	High affinity; fast binding
1	0.25	0.80 ± 0.05	Very high affinity; fast diffusing binding
1	0	1	No unbinding

RESULTS

LH dynamic binding triggers chromatin structural transitions

Fluorescence recovery after photobleaching (FRAP) experiments revealed that LHs bind dynamically, and there are different binding populations (16,17). However, due to experimental difficulties, there is only one report of specific association and dissociation rate constants (k_{on} and k_{off}) (62), indicating that k_{on} is ≈10 times higher than k_{off}.

Our uniform and non-uniform linker DNA fibers where LHs bind/unbind mimic different scenarios (Table 2). Fast diffusing, LHs have very high affinity; fast binding, LHs have high affinity; intermediate binding, LHs have moderate affinity; slow binding, LHs have a low affinity; and very slow binding, LHs have very low affinity. As LHs bind with higher affinity and rebind faster after dissociation (high P_{bind} and low P_{unb}), their effective average density in the chromatin fiber increases according to Equation (2), and as shown in Supplementary Figure S5. Fast and slow binding refers to the MC steps it takes an LH to rebind. These numbers of steps for binding and unbinding are determined implicitly through the combination of the binding/ unbinding probabilities. This can be seen in Supplementary Figure S6, which displays the presence/ absence of LH in a single nucleosome i across simulations with different P_{bind};P_{unb} combinations. We additionally consider the two extreme cases in which LHs do not bind or do not unbind ($\rho = 0$ or 1).

Figure 1A shows how the fibers condense as a function of effective average ρ for the systems with various linker DNA values: 26_D, 35_D, 44_D, 53_D, 62_D, 70_D, 80_D and nu_D, (Table 1).

In agreement with our previous results for 50-nucleosome fibers with fixed LH (35), higher affinity and faster LH binding (higher ρ), induces in most systems a structural transition: fibers become more compact and regular, losing their globular and loose shape. Such compaction trends strongly depend on the linker DNA length.

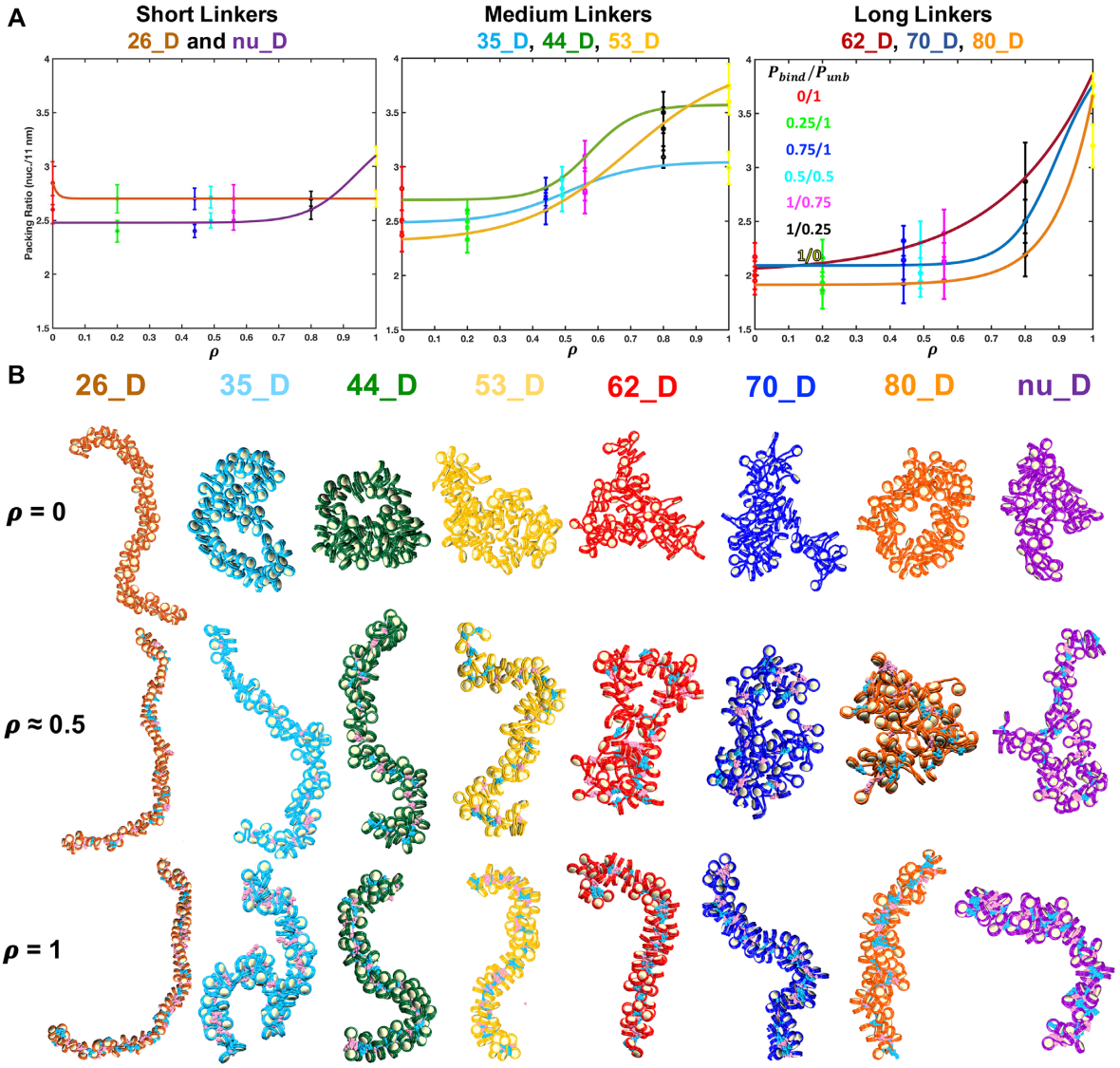

Figure 1. Dynamic LH binding affects chromatin compaction and architecture. (**A**) Average packing ratio as a function of effective average ρ for the fiber systems 26_D, 35_D, 44_D, 53_D, 62_D, 70_D, 80_D and nu_D (Table 1). (**B**) Fiber configurations for the same systems as in (A) at $\rho = 0$, $\rho \approx 0.5$ and $\rho = 1$. LH H1E is shown in cyan and H1C in pink, with bead size increased 2×. Histone tails are omitted for clarity.

Systems with medium length linkers, 35_D, 44_D and 53_D, show a sigmoidal trend with a clear transition point. Fitting of the data to an equation of the type:

$$\mathbf{Pr}(x) = a + (b - a) / \left(1 + 10^{((c-x)*d)}\right), \quad (8)$$

reveals transition points at 0.50 ± 0.18, 0.57 ± 0.12 and 0.58 ± 0.10, respectively. In Equation (8), a and b are the lower and upper asymptotes, c is the inflection point, and d is the slope of the curve at its midpoint.

Figure 1B shows fiber configurations for each system at increasing ρ. Systems 35_D, 44_D and 53_D undergo a clear transition from a globular/loose to a straight/rigid structure driven by LH binding as the effective ρ increases. At around $\rho = 0.5$, the fiber configurations are in an intermediate state between the configurations obtained at $\rho = 0$ and $\rho = 1$. Figure 2 shows the effect of LH on the average and cumulative linker DNA positions in a single nucleosome across a single trajectory. The 44 bp linker DNA positional distribution is constrained when LH binds dynamically ($\rho \approx 0.5$) compared to no LH binding ($\rho = 0$), and this effect is further increased when LH is fixed to the nucleosome ($\rho = 1$). These linkers have a length of ≈13 nm, similar to the 10 nm LH CTD when extended (47), and thus a rigid DNA stem is formed, explaining the well-defined transition point in 35_D, 44_D and 53_D.

In contrast, the 26_D fiber with short linkers shows no change in packing ratio with ρ (Figure 1A). The fiber adopts an ordered ladder-like structure that is not affected by LH biding (Figure 1B), and is consistent with the crystal structure of a four-nucleosome array lacking LH (63). Similarly, the linker DNA positional distribution (Figure 2) is not affected when LH binds dynamically ($\rho \approx 0.5$) and is only slightly affected when LH is fixed ($\rho = 1$). This is because such linkers are ≈ 6 nm long, much shorter than the CTD.

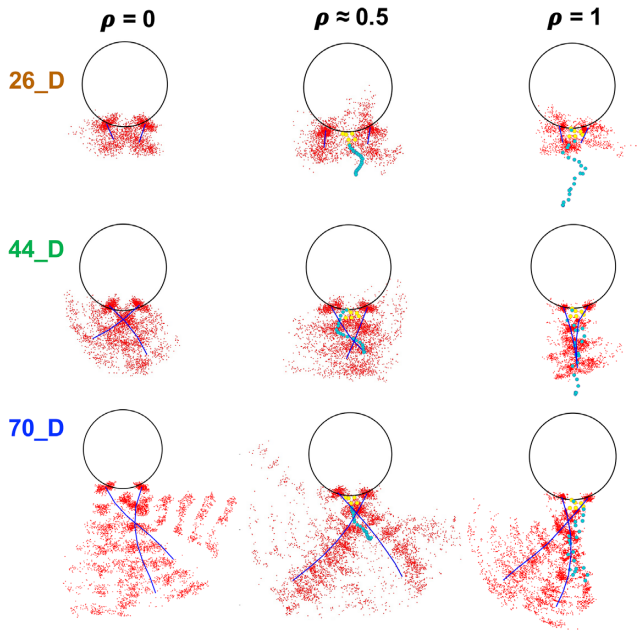

Figure 2. Linker DNA positional distributions restricted by LH binding. Nucleosome projections for 26_D, 44_D and 70_D systems showing average (blue lines) and cumulative (red dots) linker DNA positions across a single trajectory for chromatosomes without LH ($\rho = 0$, left), with dynamic LH binding ($\rho \approx 0.5$, middle), and with static LH ($\rho = 1$, right). The average positions for LH globular domain beads are shown in yellow and for CTD beads in cyan.

Thus, a tight DNA stem cannot form, and the fiber architecture is defined independently of LH.

For a different reason, long linker fibers 62_D, 70_D and 80_D do not reveal a transition point (Figure 1A). At $\rho \approx 0.5$, the three systems appear similar to fibers without LH (Figure 1B) and only at $\rho = 1$ is the straight and ordered folding reached. In agreement, the nucleosome projection in Figure 2 shows that only at $\rho = 1$, the linker DNA positional distribution is narrowed. Thus, because the linkers are too long (≈8 nm longer than the CTD) and flexible, they cannot be effectively compacted by dynamic LH, and a tight stem structure cannot be achieved.

Similar results are obtained for the non-uniform fiber that has linker DNAs of every length (Figure 1A). In this case, the short linkers cannot be compacted by LH and the long linkers are only slightly affected by LH. Thus, no transition point is evident, and only upon LH saturation, does the fiber appear rigid and straight (Figure 1B).

Overall, these results demonstrate that chromatin structural transitions triggered by dynamic LH binding occur around $\rho = 0.5$ and strongly depend on the linker DNA length. The linker DNAs most commonly found in Nature, such as 35, 44 and 52 bp, are those in which chromatin transitions are most tightly regulated by LH binding.

Associated mechanism

Figure 3A shows that the structural transition is also manifested by changes in the folding motifs. For the 26_D, 44_D and 70_D systems, we obtain internucleosome interactions typical of zigzag topology and hierarchical loops (stacked loops (37)), which are characterized by medium-range $i \pm 2$, 5 and long range $i \pm \geq 7$ contacts, respectively. As described previously (37), hierarchical looping is a higher order folding in which loops stack in 3D space, like rope flaking used in mountaineering. While more zigzag contacts indicate a straighter and ordered ladder-like structure, more hierarchical loops indicate a more globular and loose fiber.

In agreement with the compaction results, 26_D reveals almost no change in zigzag interactions with increasing ρ and a lack of hierarchical loops at every ρ. These trends reflect the ladder–like structure independent of LH binding. The 44_D and 70_D fibers exhibit different trends. There is an overall increase of zigzag interactions and a decrease of hierarchical loops with ρ, mirroring the structural transition to an ordered, less globular structure. While the 44_D fiber shows a steady increase in zigzag interactions, the 70_D system shows a sharp increase from $\rho \approx 0.8$ to $\rho = 1$. On the other hand, hierarchical looping decreases steadily in both cases.

Figure 3B shows fiber configurations for 70_D at $\rho = 1$ and $\rho \approx 0.5$, mirroring these changes in internucleosme interactions. While the fiber appears compact and ordered with a strong zigzag topology and absence of loops at $\rho = 1$, at $\rho \approx 0.5$ there are many loops and the fiber is globular and disordered.

Chromatin local geometry further clarifies the mechanism responsible for the structural transition. Figure 4A shows how the DNA entry-exit angle changes as a function of ρ for 26_D, 44_D and 70_D. Fiber 26_D shows almost no change in the DNA entry-exit angle and only upon LH saturation: the distribution plot peak shifts to smaller values but remains large, with a median of 80º. On the other hand, the 44_D fiber shows a much smaller entry-exit angle of around 50° whose probability steadily increases with ρ, indicating the formation of tighter DNA stems upon higher LH binding. The 70_D system shows a more heterogeneous trend with a peak at around 70°. Due to the high DNA flexibility, a significant difference is observed only upon LH saturation. Similar trends are observed for the nucleosome triplet angles and nucleosome dimer distances (Supplementary Figure S7). Namely, 26_D shows no significant changes in triplet angles, 44_D shows a large and steady decrease with ρ, and 70_D shows a large decrease only upon LH saturation. Finally, 26_D and 44_D show a decrease of dimer distance with ρ, with a larger effect in the latter, and 70_D shows a decrease only upon LH saturation. The correlation analysis for the median of each geometrical parameter at each ρ (Supplementary Table S3) indicates that the reduction of entry/exit and triplet angles is correlated but the dimer distance is not. Thus, LH binding compacts chromatin by reducing the DNA entry/exit angle and nucleosome triplet angle, whereas the reduction of the dimer distance follows indirectly from changes in fiber compaction.

Figure 4B shows how LHs interact with linker DNA and H3 histone tails interact with non parental cores at increasing ρ. For all three systems, LHs interact with very high frequency with their parental DNA (linker DNA belongs to the same nucleosome as LH) whereas their interaction with non parental DNA (linker DNA belongs in different chromatosome) increases with ρ. Thus, LH triggers the structural transition not only by forming tight DNA stems but

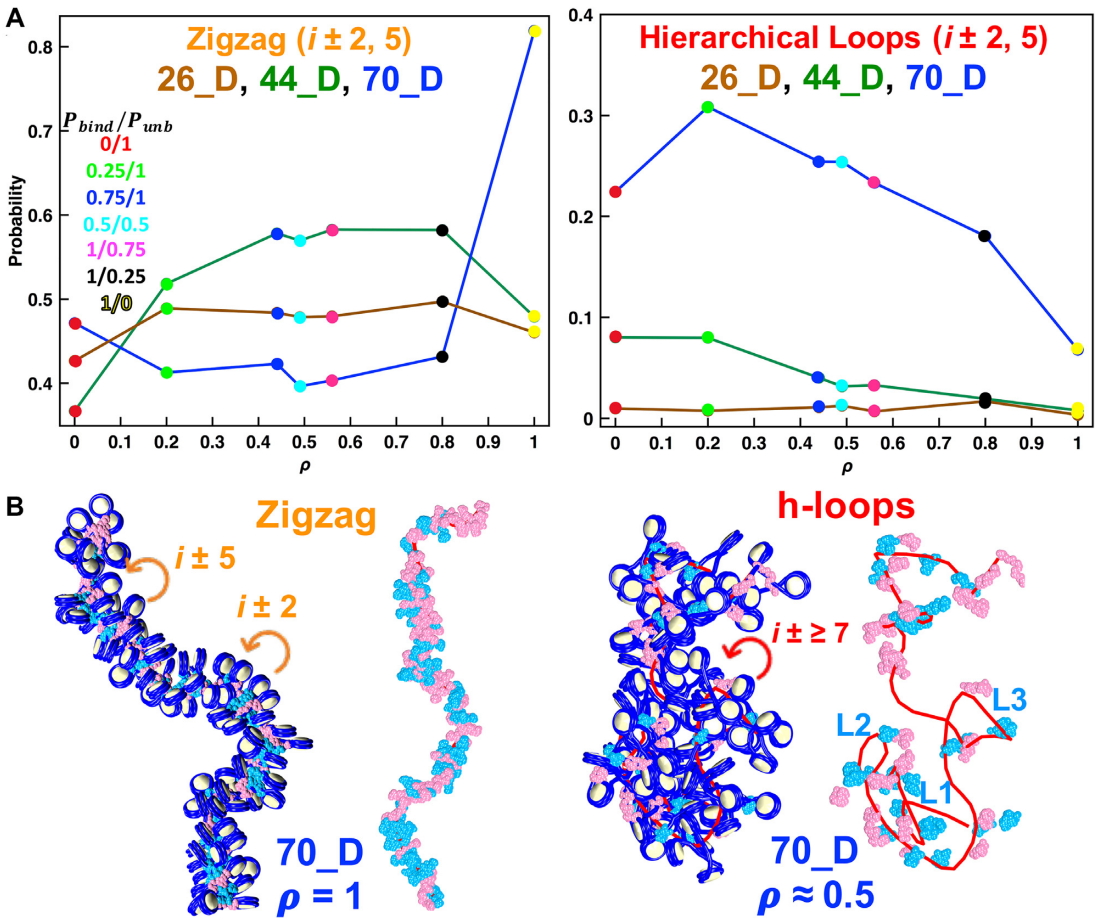

Figure 3. Dynamic LH binding affects chromatin folding motifs. (**A**) Internucleosome interactions frequencies as a function of ρ that characterize chromatin zigzag topology ($i \pm 2, 5$) and hierarchical loops ($i \pm \geq 7$) for 26_D (brown), 44_D (green), and 70_D (blue). (**B**) Fiber configurations for 70_D at $\rho = 1$ and $\rho \approx 0.5$, highlighting the strong zigzag topology and hierarchical loops, respectively. Fibers are also represented by their contour in red with LH H1E in cyan and H1C in pink, with bead size increased 2X. $k \pm 2, 5$ and ≥ 7 contacts are marked by orange and red arrows, respectively.

also by reducing the electrostatic repulsion between linker DNAs belonging to different nucleosomes. H3 tail interactions with non parental cores significantly increase with ρ for 44_D, slightly increase for 26_D, and almost do not change for 70_D, indicating that they also mediate chromatin structural transitions.

Overall, these results show how depending on the linker DNA length, LH modulates chromatin condensation through local and global structural features. In general, at low ρ, DNA stems are not well defined, and open globular fibers are dominant. At high ρ, more tight DNA stems form, producing compact fibers with strong zigzag topology and less hierarchical loops.

Static versus dynamic LH binding and modulation by internal and external parameters

We further study three systems above (nu_D, 44_D and 70_D) with static LH for comparison.

Figure 5A shows that the packing ratio of nu_S, 44_S and 70_S also increases with ρ. However, the changes are more gradual than with dynamic LH binding, and no transition point is evident for any of linker length. In general, static LH compacts chromatin to a greater extent than dynamic LH, especially in the case of long linkers (70_S versus 70_D). Figure 5B shows that when ρ is similar, the fiber configurations obtained with static and dynamic LH are comparable. Yet, dynamic LH fibers appear less folded, in agreement with our previous studies showing that LH dynamic binding facilitates fiber unfolding compared to static LH (24,25).

To further investigate how chromatin parameters and ionic environment regulate the structural transitions, we simulate static LH systems nu_S, 44_S and 70_S in different conditions, such as low and high salt instead of physiological salt, phosphorylated instead of wildtype LH, truncated instead of wildtype histone tails, and off instead of on-dyad LH binding mode.

As shown in Figure 6A, at low salt concentration, all three systems nu_S_L, 44_S_L and 70_S_L have lower packing ratios at every ρ compared to physiological salt (nu_S, 44_S and 70_S), confirming the role of salt concentration in chromatin folding (64). Fiber compaction increases rapidly with ρ, likely due to a stronger interaction between LH and linker DNA in this condition (65). However, even at $\rho = 1$ these values are similar to the packing ratios obtained at physiological salt concentrations without LH, indicating

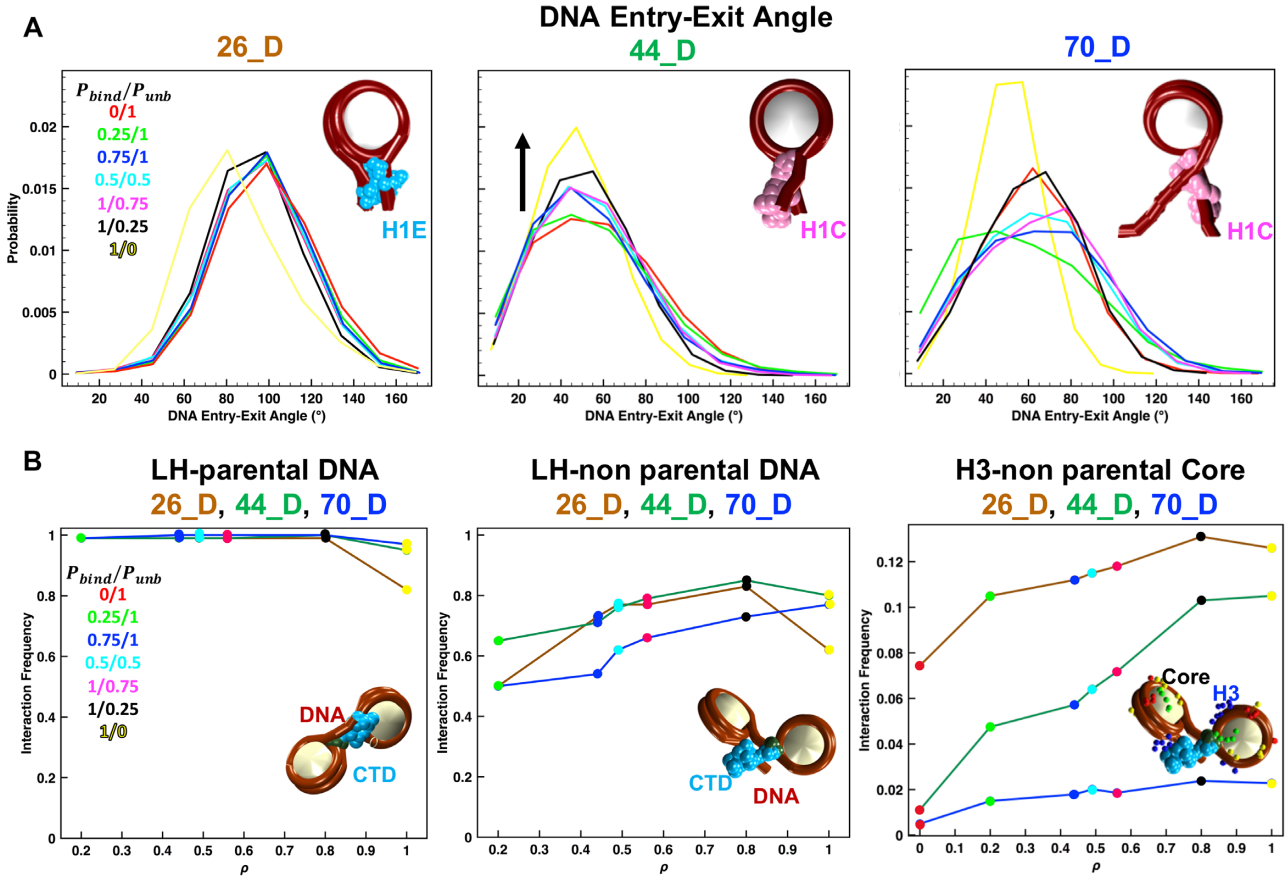

Figure 4. Local fiber geometry and histone interactions mediate structural transitions. (**A**) Probability distributions for linker DNA entry-exit angle as a function of ρ calculated for systems with dynamic LH binding: 26_D, 44_D and 70_D. (**B**) Frequency of the interactions between LH and parental DNA (left), LH and non parental DNA (middle), and H3 tails and non parental cores (right) calculated for the same systems as in (A).

that fibers remain unfolded: see fiber configurations in Figure 6B. Similar results are obtained for nu_S_L and 70_S_L (Supplementary Figure S8).

At high salt, systems nu_S_H, 44_S_H and 70_S_H are more compact at every ρ compared to physiological salt concentration (Figure 6A). The effect of LH is less pronounced in the nu_S_H and 44_S_H, likely due to the competition between LH and Mg^{2+}. In contrast, 70_S_H exhibits a sharp increase in compaction. As shown in Figure 6B, the 44_S_H fiber architecture is straighter and more rigid, even at low ρ, compared to fibers in physiological salt concentrations.

Phosphorylation of LH is a post translational modification associated with changes in chromatin condensation levels (66). In agreement, phosphorylated fibers are less compact at every ρ compared to wildtype fibers (Figure 6A). 44_S_P reaches a plateau in the packing ratio at around $\rho = 0.7$, while in the wildtype fiber, packing ratio continues to increase up to $\rho = 1$. The nu_S_P fiber condensation is almost not affected by ρ. And packing ratio of 70_S_P increases steadily up to $\rho = 0.9$, where a plateau is reached. Phosphorylated fibers also appear to have less self-association than wildtype fibers (Figure 6B).

When histone tails are removed, nu_S_T, 44_S_T and 70_S_T completely unfold at low ρ and have low packing ratios of 1–2 nuc./11 nm (Figure 6A). Similar to the low salt systems, higher compaction is achieved upon LH saturation, but again, these packing ratios remain similar to the values obtained for wildtype systems without LH. This results from disrupting internucleosome contacts in tail-less fibers (Supplementary Figure S9), which are not rescued by increasing ρ. Also, as mentioned above, tail interactions with non-parental nucleosome cores increase with ρ, indicating a role for the tails in the structural transition. Long-range internucleosome interactions typical of hierarchical looping are largely absent in the tail-less systems at every ρ, and the zigzag topology is mostly unaffected with ρ (Supplementary Figure S10). Thus, no transition from a globular to a straight and compact fiber occurs.

For variable LH binding modes, systems nu_S_+20, nu_S_–20, 44_S_+20, 44_S_–20, 70_S_+20 and 70_S_–20 show similar trends to the systems with on-dyad LH binding, suggesting that ρ-induced structural transitions are less sensitive to the LH binding mode. For some systems, off-dyad binding at high ρ is not as beneficial for fiber compaction as on-dyad binding, in agreement with our previous findings (48).

Overall, these results emphasize the importance of salt concentration, histone tails, and LH phosphorylation in modulating chromatin structural transitions. Low salt concentration and absence of histone tails produce unfolded fibers at low ρ. At high ρ, fibers are slightly more compact

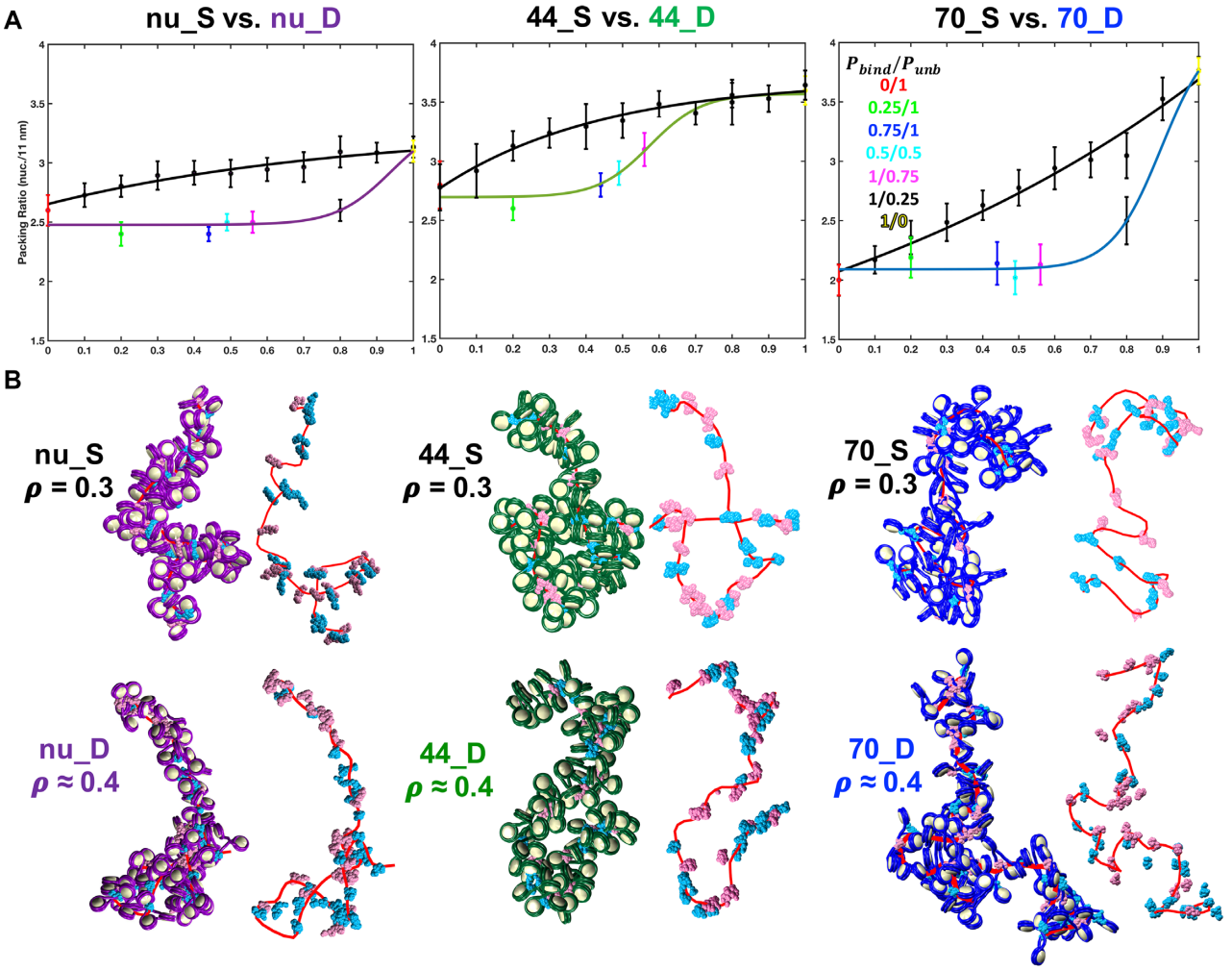

Figure 5. Static LH binding better compacts chromatin than dynamic LH binding. (**A**) Packing ratio as a function of ρ for the nu_S and nu_D, 44_S and 44_D, and 70_S and 70_D systems. (**B**) Top: Fiber configurations and their contours for systems with static LH binding nu_S, 44_S and 70_S at $\rho = 0.3$. Bottom: Fiber configurations and their contours for systems with dynamic LH binding nu_D, 44_D and 70_D at $\rho \approx 0.4$. LHs H1E are shown in cyan and H1C in pink, with bead size increased 2×. Tails are omitted for clarity.

but remain at compaction levels similar to those obtained without LH at physiological salt concentration or in presence of tails. Moreover, no significant change in hierarchical loops and zigzag topology is seen with ρ. Thus, such conditions suppress structural transitions. The effect of Mg^{2+} depends on linker DNA lengths. Namely, long linkers benefit more from Mg^{2+} than short ones. Mg^{2+} promotes a structural transition at lower ρ by producing more compact and straight fibers. The opposite effect occurs with phosphorylated LH as it decreases LH compaction capacity and delays the structural transition.

Relationship between ρ and DNA linker length

Experimental determination of ρ and DNA linker length has shown a linear correlation between both parameters, indicating a synergistic relationship (13). We further explore this aspect by studying how fibers with increasing linker DNA lengths, systems 26_S, 35_S, 44_S, 53_S, 62_S, 70_S and 80_S, are compacted at the fixed $\rho = 0.5$, as well as how increasing DNA linker length with ρ as a pair affects fiber condensation.

Figure 7A (left) shows that when different linker length fibers are simulated with $\rho = 0.5$, compaction is higher for 53_S with NRL = 200 bp. As found in our previous study (58), such NRL produces higher compaction compared to other NRLs in fibers without LH, but upon LH addition, this difference increases, indicating that LH works as a better compactor in fibers with DNA linkers of medium lengths, such as NRL = 191, 200 and 209 bp. Similar to the results with dynamic LH binding, the worst compaction is achieved in fibers with too short or too long DNA linker lengths, like NRL = 173 and 227 bp. Intermediate condensations are achieved for fibers with NRL = 182 and 218 bp. As discussed above, fibers with very short DNA linker lengths fold into ladder-like structures, which are not affected by LH binding. Arrays with medium linker DNA exhibit the highest increase in compaction upon addition of LH, while arrays with long linker DNA have heterogeneous structures where the linker DNA is bent so that rigid LH/linker DNA stems cannot form well (Figure 7B) (58).

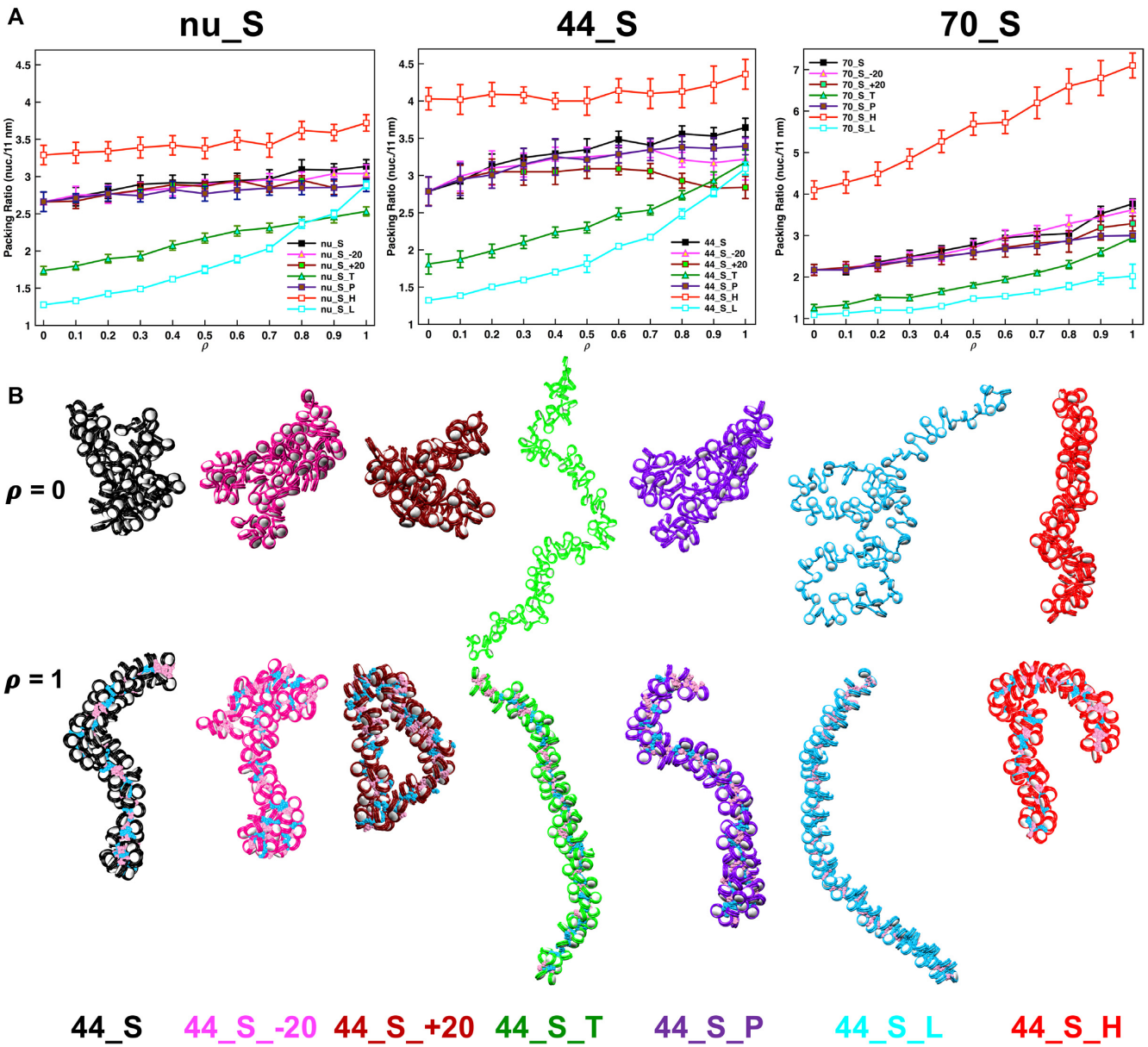

Figure 6. Internal and external parameters regulate structural transitions. (**A**) Average packing ratio as a function of ρ for chromatin fibers with three linker types (nu, 44 bp and 70 bp) in different conditions: 1) LH on-dyad: nu_S, 44_S and 70_S; 2) LH off-dyad -20°: nu_S_-20, 44_S_-20 and 70_S_-20; 3) LH off-dyad + 20°: nu_S_+20, 44_S_+20 and 70_S_+20; 4) truncated histone tails: nu_S_T, 44_S_T and 70_S_T; 5) phosphorylated LH: nu_S_P, 44_S_P and 70_S_P; 6) high salt concentration: nu_S_H, 44_S_H and 70_S_H; and 7) low salt concentration: nu_S_L, 44_S_L and 70_S_L. (**B**) Fiber configurations for the 44 bp system at $\rho = 0$ (top) and $\rho = 1$ (bottom) in the seven conditions studied. LH H1E is shown in cyan and H1C in pink, with bead size increased 2×. Nucleosome tails are omitted for clarity.

These trends are evident by our nucleosome projections for linker DNA = 53 bp (Supplementary Figure S11), showing that the length of LH CTD is almost the same as the DNA length.

Figure 7A (right) shows that for different combinations of NRL and ρ, packing ratio increases with ρ following a sigmoidal trend, indicating cooperativity between both parameters. This trend is similar to that observed for our dynamic 35_D, 44_D and 53_D systems (Figure 1A). Based on the combinations of ρ and linker DNA found in nature (13), this scenario is most likely to occur *in vivo*, where an increase in ρ produces an increase in linker DNA length. The fitting of the data to the same sigmoidal equation as used in Figure 1 provides an inflection point of 0.54 ± 0.1, similar to the values we obtained for 35_D, 44_D and 53_D.

DISCUSSION

Recent studies have emphasized the role of LH depletion in the development of diseases such as lymphoma (35) and retinal disorders (31). In this connection, we expand on our previous study on LH deficiency and lymphoma (35) by pinpointing the critical LH density that triggers chromatin structural transitions. In addition, we determine the con-

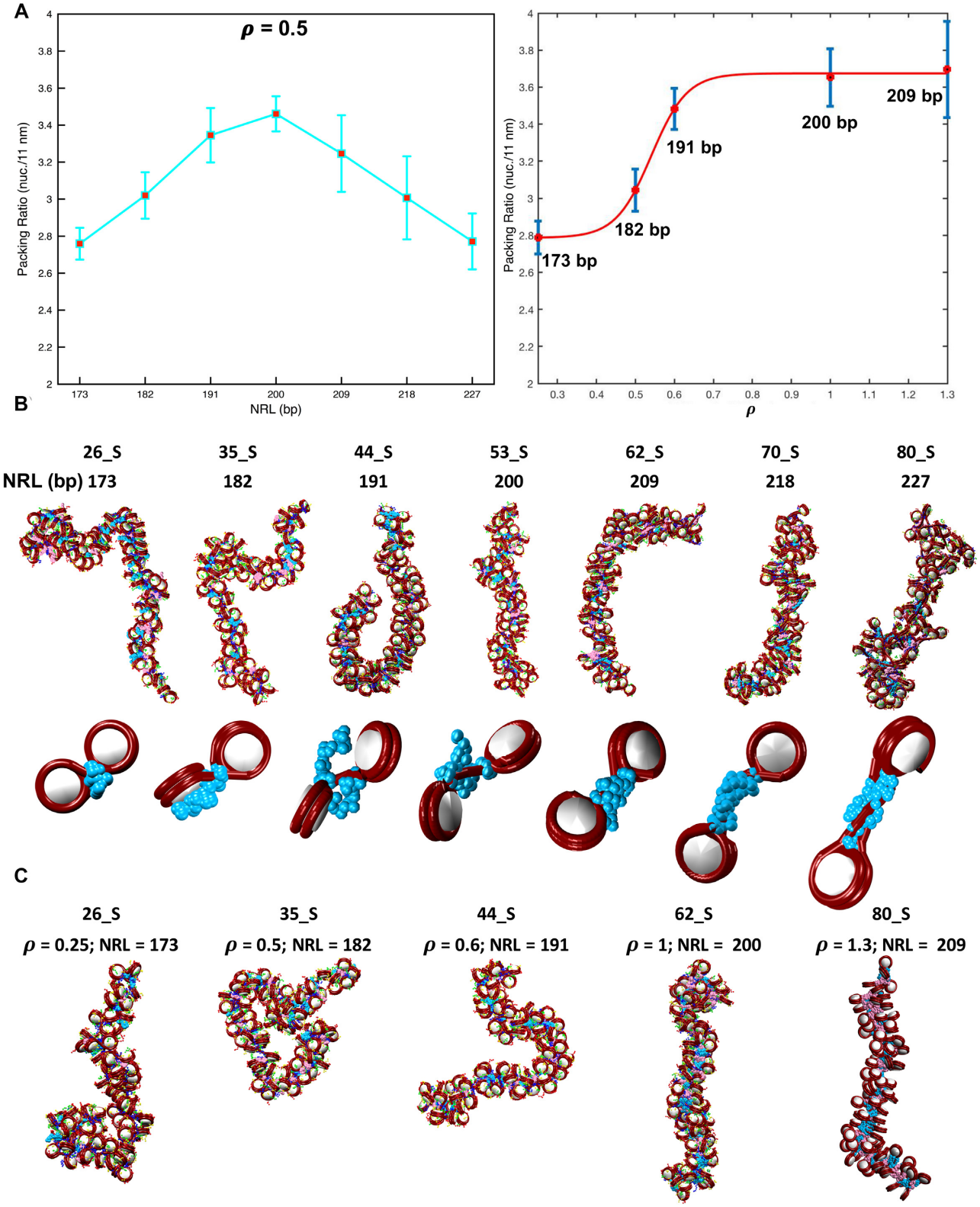

Figure 7. Chromatin condensation is related to the ρ/DNA linker length combination. (**A**) Left: packing ratio as a function of DNA linker length for fibers with static LH at $\rho = 0.5$: 26_S, 35_S, 44_S, 53_S, 62_S, 70_S and 80_S. Right: packing ratio as a function of ρ for fibers with static LH and different combinations DNA linker/ρ: 26_S, 35_S, 44_S, 62_S, and 80_S. (**B**) Representative fiber configurations for different DNA linker lengths and the corresponding dinucleosomes showing the DNA stem formation. (**C**) Representative fiber configurations for each DNA linker/ρ combination.

nection between these transitions and linker DNA lengths, and study its regulation by several chromatin parameters, such as histone tails, salt concentration, LH phosphorylation, and LH binding mode. Moreover, by introducing dynamic LH binding and studying fibers with different linker DNAs in several fast/slow binding scenarios, we capture and explain mechanistically how LH triggers chromatin structural transitions.

For most of the fiber conditions studied, higher LH affinity and faster binding triggers a structural transition where fibers become more rigid and compact and less globular and loose. Thus, the presence in nature of different LH binding populations could be related to the local regulation of the chromatin fiber where the slow binding population induces an open state that is easily transcribed, whereas the fast-binding population induces a repressed closed state. Consistent with this idea, LH in heterochromatin displays long retention times (16).

For the medium linker length systems 35_D, 44_D and 53_D, a clear transition point around $\rho = 0.5$ is observed. The mechanism behind such transition is formation of rigid DNA stems upon LH binding, which constrains the linker DNA positional distribution, and is optimal when the length of the linker DNA and the LH CTD are similar. In extreme cases, where the linker DNA is too short, the transition does not occur due to an imbalance between linker DNA and LH lengths. In agreement, Routh et al.'s sedimentation velocities (67) for arrays with NRL = 197 bp as a function of ρ revealed a sigmoidal trend similar to our Figure 1 but a linear trend for arrays with NRL = 167 bp. While the authors do not report the value of the transition point, visual inspection of the plot indicates that it occurs at around $\rho = 0.5$. Similar results were also obtained by Song et al. for nucleosome arrays of NRL = 177 bp (68).

In nature, ρ and linker DNA length are tightly modulated (13). Thus, regulation of chromatin transitions by the specific combination of these two parameters could provide an additional level of epigenetic regulation. For example, chromatin transitions towards loose fibers triggered by LH depletion are consistent with findings showing that transcriptionally active chromatin presents low ρ (13). In mouse rod photoreceptors, the gradual increase of linker DNA and ρ during retina maturation is a key mechanism for regulating chromatin condensation (31). Alterations of heterochromatin formation in these cells leads to progressive loss of functionality, with associated retinal disorder diseases (40). Similarly, in lymphoma of B cells, LH depletion affects chromatin compartmentalization with a transition from repressed to active compartments, inducing aberrant gene expression (35). Thus, a mechanism in which linker DNA, ρ, or both are altered to shift the structural transition point and thus define an open or closed chromatin state can define the cell's fate.

Mammals have 11 LH variants with a highly conserved globular domain but more variable N- and C-terminal domains (69). As we have shown, the highest compaction is achieved for linker DNA lengths near the CTD length. With this mechanism, we expect the different variants to optimally condense fibers with linker DNA lengths similar in size to their CTD length, and thus, induce chromatin transitions differently. For example, among the somatic variants H1a to H1e, H1a and H1c have the shortest CTDs, while H1b and H1e have the longest CTDs. Thus, H1a and H1c should be better condensers and transition triggers of medium linker DNA fibers, such as 30 or 44 bp, while H1b and H1e could work better with longer linker DNAs, such as 53–80 bp. Similar effects of LH variants on nucleosome spacing have been observed (70,71). Clausell et al. showed that addition of H1b and H1e variants to minichromosomes produces relocation of nucleosomes and the highest increase in linker DNA length, while the addition of H1a and H1c produces a more moderate increase (70). Also, Öberg et al. demonstrated that adding H1e to oocytes increases the linker DNA length by 13–20 bp, while adding H1c produces a more moderate increase of 4.5–7 bp (71).

The role of histone tails in mediating nucleosome interactions is well appreciated (53,72). Here, we showed that nucleosome arrays without histone tails are unfolded at every ρ, thereby eliminating chromatin structural transitions. Thus, post translational modifications of histone tails likely play a role in regulating structural transitions. Indeed, a reduction of H4 acetylation has been observed for LH depleted embryonic stem cells, probably to counteract LH loss (73).

Similarly, the role of salt concentration on chromatin folding is a well-known factor (41). Our simulations at 15 mM NaCl show that although LH can compact the fibers, they remain unfolded even at high ρ. At high salt concentrations, however, a high level of compaction can be reached even at low ρ, and the fiber's global shape is more straight and less globular. Thus, while low salt concentration impairs the transition, high concentration promotes it.

We also showed that phosphorylated LH condenses chromatin less efficiently. Because CTD partial phosphorylation affects its DNA binding affinity (74) and LH binding dynamics (19), CTD phosphorylation impairs chromatin structural transitions. This agrees with LH phosphorylation levels becoming maximal during the metaphase cell state (75), when chromatin fibers are globular and loose (37), and highly transcribed (76).

That LH triggers structural transitions in different fibers through a DNA stem formation mechanism and its modulation by several elements offers a new epigenetic mechanism by which LH could regulate accessibility of the transcription machinery to gene elements. The link between LH-deficient chromatin and lymphoma tendency is known (35) but the relationship is far from clear. For lymphoma and other human diseases associated with vision (40), further studies are needed to understand the epigenetic basis of these disorders. The modulators and mechanisms identified here could define potential avenues for diagnostic and therapeutic intervention.

DATA AVAILABILITY

Analysis scripts are publicly available on GitHub at the following address: https://github.com/sp5413/Chromatin_Transitions_LH.

SUPPLEMENTARY DATA

Supplementary Data are available at NAR Online.

ACKNOWLEDGEMENTS

We thank Dr Ari Melnick and his group at Weill Cornell Medicine for motivating us to explore the role of linker histone in chromatin structural transitions. Assistance with coding is also acknowledged to Dr Zilong Li.

Author contribution: S. Portillo-Ledesma conceived the study, performed simulations, analysis and wrote the article. M. Wagley performed simulations and analysis. T. Schlick conceived the study, wrote the article and acquired funding.

FUNDING

T. Schlick is grateful to the National Institutes of Health, National Institutes of General Medical Sciences Award [R35-GM122562]; National Science Foundation RAPID Award [2030377] from the Division of Mathematical Sciences, and to Philip-Morris USA Inc.; NYU IT High Performance Computing resources, services, and staff expertise (in part). Funding for open access charge: NIH [R35-GM122562].

Conflict of interest statement. The authors declare that the research was conducted in the absence of any commercial or financial relationships that could be construed as a potential conflict of interest.

REFERENCES

1. Maeshima,K., Tamura,S., Hansen,J.C. and Itoh,Y. (2020) Fluid-like chromatin: toward understanding the real chromatin organization present in the cell. *Curr. Opin. Cell Biol.*, **64**, 77–89.
2. Rowley,M.J. and Corces,V.G. (2018) Organizational principles of 3D genome architecture. *Nat. Rev. Genet.*, **19**, 789–800.
3. Grigoryev,S.A., Arya,G., Correll,S., Woodcock,C.L. and Schlick,T. (2009) Evidence for heteromorphic chromatin fibers from analysis of nucleosome interactions. *Proc. Natl. Acad. Sci. U.S.A.*, **106**, 13317–13322.
4. Ricci,M.A., Manzo,C., García-Parajo,M.F., Lakadamyali,M. and Cosma,M.P. (2015) Chromatin fibers are formed by heterogeneous groups of nucleosomes in vivo. *Cell*, **160**, 1145–1158.
5. Krietenstein,N., Abraham,S., Venev,S.V., Abdennur,N., Gibcus,J., Hsieh,T.H.S., Parsi,K.M., Yang,L., Maehr,R., Mirny,L.A. *et al.* (2020) Ultrastructural details of mammalian chromosome architecture. *Mol. Cell*, **78**, 554–565.
6. Gómez-García,P.A., Portillo-Ledesma,S., Neguembor,M.V., Pesaresi,M., Oweis,W., Rohrlich,T., Wieser,S., Meshorer,E., Schlick,T., Cosma,M.P. *et al.* (2021) Mesoscale modeling and single-nucleosome tracking reveal remodeling of clutch folding and dynamics in stem cell differentiation. *Cell Rep.*, **34**, 108614.
7. Portillo-Ledesma,S., Tsao,L.H., Wagley,M., Lakadamyali,M., Cosma,M.P. and Schlick,T. (2021) Nucleosome clutches are regulated by chromatin internal parameters. *J. Mol. Biol.*, **433**, 166701.
8. Dekker,J. and Heard,E. (2015) Structural and functional diversity of topologically associating domains. *FEBS Lett.*, **589**, 2877–2884.
9. Fudenberg,G., Imakaev,M., Lu,C., Goloborodko,A., Abdennur,N. and Mirny,L.A. (2016) Formation of chromosomal domains by loop extrusion. *Cell Rep.*, **15**, 2038–2049.
10. Lieberman-Aiden,E., Van Berkum,N.L., Williams,L., Imakaev,M., Ragoczy,T., Telling,A., Amit,I., Lajoie,B.R., Sabo,P.J., Dorschner,M.O. *et al.* (2009) Comprehensive mapping of long-range interactions reveals folding principles of the human genome. *Science*, **326**, 289–293.
11. Cremer,T. and Cremer,M. (2010) Chromosome territories. *Cold Spring Harb. Perspect. Biol.*, **2**, a003889.
12. Bednar,J., Horowitz,R.A., Grigoryev,S.A., Carruthers,L.M., Hansen,J.C., Koster,A.J. and Woodcock,C.L. (1998) Nucleosomes, linker DNA, and linker histone form a unique structural motif that directs the higher-order folding and compaction of chromatin. *Proc. Natl. Acad. Sci. U.S.A.*, **95**, 14173–14178.
13. Woodcock,C.L., Skoultchi,A.I. and Fan,Y. (2006) Role of linker histone in chromatin structure and function: H1 stoichiometry and nucleosome repeat length. *Chromosom. Res.*, **14**, 17–25.
14. Willcockson,M.A., Healton,S.E., Weiss,C.N., Bartholdy,B.A., Botbol,Y., Mishra,L.N., Sidhwani,D.S., Wilson,T.J., Pinto,H.B., Maron,M.I. *et al.* (2021) H1 histones control the epigenetic landscape by local chromatin compaction.*Nature*, **589**, 293–298.
15. Fyodorov,D.V, Zhou,B.-R., Skoultchi,A.I. and Bai,Y. (2018) Emerging roles of linker histones in regulating chromatin structure and function. *Nat. Rev. Mol. Cell. Biol.*, **19**, 192–206.
16. Misteli,T., Gunjan,A., Hock,R., Bustin,M. and Brown,D.T. (2000) Dynamic binding of histone H1 to chromatin in living cells. *Nature*, **408**, 877–881.
17. Lever,M.A., Th'ng,J.P.H., Sun,X. and Hendzel,M.J. (2000) Rapid exchange of histone H1.1 on chromatin in living human cells. *Nature*, **408**, 873–876.
18. Dou,Y., Bowen,J., Liu,Y. and Gorovsky,M.A. (2002) Phosphorylation and an ATP-dependent process increase the dynamic exchange of H1 in chromatin. *J. Cell Biol.*, **158**, 1161–1170.
19. Contreras,A., Hale,T.K., Stenoien,D.L., Rosen,J.M., Mancini,M.A. and Herrera,R.E. (2003) The dynamic mobility of histone H1 is regulated by Cyclin/CDK phosphorylation. *Mol. Cell. Biol.*, **23**, 8626–8636.
20. Gong,M., Ni,J.H. and Jia,H.T. (2002) Increased exchange rate of histone H1 on chromatin by exogenous myogenin expression. *Cell Res.*, **12**, 395–400.
21. D.T.,B., T.,I., T.,M., Brown,D.T., Izard,T. and Misteli,T. (2006) Mapping the interaction surface of linker histone H1(0) with the nucleosome of native chromatin in vivo. *Nat. Struct. Mol. Biol.*, **13**, 250–255.
22. Becker,M., Becker,A., Miyara,F., Han,Z., Kihara,M., Brown,D.T., Hager,G.L., Latham,K., Adashi,E.Y. and Misteli,T. (2005) Differential in vivo binding dynamics of somatic and oocyte-specific linker histones in oocytes and during ES cell nuclear transfer. *Mol. Biol. Cell*, **16**, 3887–3895.
23. Th'ng,J.P.H., Sung,R., Ye,M. and Hendzel,M.J. (2005) H1 family histones in the nucleus: control of binding and localization by the C-terminal domain. *J. Biol. Chem.*, **280**, 27809–27814.
24. Collepardo-Guevara,R. and Schlick,T. (2011) The effect of linker histone's nucleosome binding affinity on chromatin unfolding mechanisms. *Biophys. J.*, **101**, 1670–1680.
25. Collepardo-Guevara,R. and Schlick,T. (2012) Crucial role of dynamic linker histone binding and divalent ions for DNA accessibility and gene regulation revealed by mesoscale modeling of oligonucleosomes. *Nucleic Acids Res.*, **40**, 8803–8817.
26. Happel,N. and Doenecke,d,D. (2009) Histone H1 and its isoforms: contribution to chromatin structure and function. *Gene*, **431**, 1–12.
27. Fan,Y., Sirotkin,A., Russell,R.G., Ayala,J. and Skoultchi,A.I. (2001) Individual somatic H1 subtypes are dispensable for mouse development even in mice lacking the H1 0 replacement subtype. *Mol. Cell. Biol.*, **21**, 7933–7943.
28. Sirotkin,A.M., Edelmann,W., Cheng,G., Klein-Szanto,A., Kucherlapati,R. and Skoultchi,A.I. (1995) Mice develop normally without the H10 linker histone. *Proc. Natl. Acad. Sci. U.S.A.*, **92**, 6434–6438.
29. Zhang,Y., Cooke,M., Panjwani,S., Cao,K., Krauth,B., Ho,P.Y., Medrzycki,M., Berhe,D.T., Pan,C., McDevitt,T.C. *et al.* (2012) Histone H1 depletion impairs embryonic stem cell differentiation. *PLoS Genet.*, **8**, e1002691.
30. Fan,Y., Nikitina,T., Morin-Kensicki,E.M., Zhao,J., Magnuson,T.R., Woodcock,C.L. and Skoultchi,A.I. (2003) H1 linker histones are essential for mouse development and affect nucleosome spacing in vivo. *Mol. Cell. Biol.*, **23**, 4559–4572.
31. Popova,E.Y., Grigoryev,S.A., Fan,Y., Skoultchi,A.I., Zhang,S.S. and Barnstable,C.J. (2013) Developmentally regulated linker histone H1c promotes heterochromatin condensation and mediates structural integrity of rod photoreceptors in mouse retina. *J. Biol. Chem.*, **288**, 17895–17907.
32. Okosun,J., Bödör,C., Wang,J., Araf,S., Yang,C.Y., Pan,C., Boller,S., Cittaro,D., Bozek,M., Iqbal,S. *et al.* (2014) Integrated genomic analysis identifies recurrent mutations and evolution patterns driving the initiation and progression of follicular lymphoma. *Nat. Genet.*, **46**, 176–181.
33. Li,H., Kaminski,M.S., Li,Y., Yildiz,M., Ouillette,P., Jones,S., Fox,H., Jacobi,K., Saiya-Cork,K., Bixby,D. *et al.* (2014) Mutations in linker

histone genes HIST1H1 b, c, d, and E; OCT2 (POU2F2); IRF8; and ARID1A underlying the pathogenesis of follicular lymphoma. *Blood*, **123**, 1487–1498.
34. Reichel,J., Chadburn,A., Rubinstein,P.G., Giulino-Roth,L., Tam,W., Liu,Y., Gaiolla,R., Eng,K., Brody,J., Inghirami,G. *et al.* (2015) Flow sorting and exome sequencing reveal the oncogenome of primary hodgkin and reed-sternberg cells. *Blood*, **125**, 1061–1072.
35. Yusufova,N., Kloetgen,A., Teater,M., Osunsade,A., Camarillo,J.M., Chin,C.R., Doane,A.S., Venters,B.J., Portillo-Ledesma,S., Conway,J. *et al.* (2021) Histone H1 loss drives lymphoma by disrupting 3D chromatin architecture. *Nature*, **589**, 299–305.
36. Gibson,B.A., Doolittle,L.K., Schneider,M.W.G., Jensen,L.E., Gamarra,N., Henry,L., Gerlich,D.W., Redding,S. and Rosen,M.K. (2019) Organization of chromatin by intrinsic and regulated phase separation. *Cell*, **179**, 470–484.
37. Grigoryev,S.A., Bascom,G., Buckwalter,J.M., Schubert,M.B., Woodcock,C.L. and Schlick,T. (2016) Hierarchical looping of zigzag nucleosome chains in metaphase chromosomes. *Proc. Natl. Acad. Sci. U.S.A.*, **113**, 1238–1243.
38. Diesinger,P.M. and Heermann,D.W. (2009) Depletion effects massively change chromatin properties and influence genome folding. *Biophys. J.*, **97**, 2146–2153.
39. Diesinger,P.M., Kunkel,S., Langowski,J. and Heermann,D.W. (2010) Histone depletion facilitates chromatin loops on the kilobasepair scale. *Biophys. J.*, **99**, 2995–3001.
40. Helmlinger,D., Hardy,S., Abou-Sleymane,G., Eberlin,A., Bowman,A.B., Gansmüller,A., Picaud,S., Zoghbi,H.Y., Trottier,Y., Tora,L. *et al.* (2006) Glutamine-expanded ataxin-7 alters TFTC/STAGA recruitment and chromatin structure leading to photoreceptor dysfunction. *PLoS Biol*., **4**, 0432–0445.
41. Sun,J., Zhang,Q. and Schlick,T. (2005) Electrostatic mechanism of nucleosomal array folding revealed by computer simulation. *Proc. Natl. Acad. Sci. U.S.A.*, **102**, 8180–8185.
42. Beard,D.A. and Schlick,T. (2001) Computational modeling predicts the structure and dynamics of chromatin fiber. *Structure*, **9**, 105–114.
43. Beard,D.A. and Schlick,T. (2001) Modeling salt-mediated electrostatics of macromolecules: the discrete surface charge optimization algorithm and its application to the nucleosome. *Biopolymers*, **58**, 106–115.
44. Arya,G., Zhang,Q. and Schlick,T. (2006) Flexible histone tails in a new mesoscopic oligonucleosome model. *Biophys. J.*, **91**, 133–150.
45. Jian,H., Vologodskii,A.V. and Schlick,T. (1997) A combined wormlike-chain and bead model for dynamic simulations of long linear DNA. *J. Comput. Phys.*, **136**, 168–179.
46. Stigter,D. (1977) Interactions of highly charged colloidal cylinders with applications to double-stranded DNA. *Biopolymers*, **16**, 1435–1448.
47. Luque,A., Collepardo-Guevara,R., Grigoryev,S. and Schlick,T. (2014) Dynamic condensation of linker histone C-terminal domain regulates chromatin structure. *Nucleic Acids Res*., **42**, 7553–7560.
48. Perišić,O., Portillo-Ledesma,S. and Schlick,T. (2019) Sensitive effect of linker histone binding mode and subtype on chromatin condensation. *Nucleic Acids Res*., **47**, 4948–4957.
49. Allan,J., Mitchell,T., Harborne,N., Bohm,L. and Crane-Robinson,C. (1986) Roles of H1 domains in determining higher order chromatin structure and H1 location. *J. Mol. Biol.*, **187**, 591–601.
50. Sridhar,A., Farr,S.E., Portella,G., Schlick,T., Orozco,M. and Collepardo-Guevara,R. (2020) Emergence of chromatin hierarchical loops from protein disorder and nucleosome asymmetry. *Proc. Natl. Acad. Sci. U.S.A*., **117**, 7216–7224.
51. Rouzina,L. and Bloomfield,V.A. (1998) DNA bending by small, mobile multivalent cations. *Biophys. J.*, **74**, 3152–3164.
52. Baumann,C.G., Smith,S.B., Bloomfield,V.A. and Bustamante,C. (1997) Ionic effects on the elasticity of single DNA molecules. *Proc. Natl. Acad. Sci. U.S.A.*, **94**, 6185–6190.
53. Arya,G. and Schlick,T. (2009) A tale of tails: how histone tails mediate chromatin compaction in different salt and linker histone environments. *J. Phys. Chem. A*, **113**, 4045–4059.
54. Arya,G. and Schlick,T. (2006) Role of histone tails in chromatin folding revealed by a mesoscopic oligonucleosome model. *Proc. Natl. Acad. Sci. U.S.A*., **103**, 16236–16241.
55. Metropolis,N. and Ulam,S. (1949) The monte carlo method. *J. Am. Stat. Assoc.*, **44**, 335–341.
56. Rosenbluth,M.N. and Rosenbluth,A.W. (1955) Monte carlo calculation of the average extension of molecular chains. *J. Chem. Phys.*, **23**, 356–359.
57. Voong,L.N., Xi,L., Sebeson,A.C., Xiong,B., Wang,J.P. and Wang,X. (2016) Insights into nucleosome organization in mouse embryonic stem cells through chemical mapping. *Cell*, **167**, 1555–1570.
58. Perišić,O., Collepardo-Guevara,R. and Schlick,T. (2010) Modeling studies of chromatin fiber structure as a function of DNA linker length. *J. Mol. Biol.*, **403**, 777–802.
59. Sancho,M., Diani,E., Beato,M. and Jordan,A. (2008) Depletion of human histone H1 variants uncovers specific roles in gene expression and cell growth. *PLoS Genet*., **4**, e1000227.
60. Orrego,M., Ponte,I., Roque,A., Buschati,N., Mora,X. and Suau,P. (2007) Differential affinity of mammalian histone H1 somatic subtypes for DNA and chromatin. *BMC Biol*., **5**, 22.
61. Drew,H.R. and Travers,A.A. (1985) DNA bending and its relation to nucleosome positioning. *J. Mol. Biol.*, **186**, 773–790.
62. Lele,T., Wagner,S.R., Nickerson,J.A. and Ingber,D.E. (2006) Methods for measuring rates of protein binding to insoluble scaffolds in living cells: histone H1-chromatin interactions. *J. Cell. Biochem.*, **99**, 1334–1342.
63. Schalch,T., Duda,S., Sargent,D.F. and Richmond,T.J. (2005) X-ray structure of a tetranucleosome and its implications for the chromatin fibre. *Nature*, **436**, 138–141.
64. Hansen,J.C., Ausio,J., Stanik,V.H. and Van Holde,K.E. (1989) Homogeneous reconstituted oligonucleosomes, evidence for salt-dependent folding in the absence of histone h1. *Biochemistry*, **28**, 9129–9136.
65. Al-Natour,Z. and Hassan,A.H. (2007) Effect of salt on the binding of the linker histone HI to DNA and nucleosomes. *DNA Cell Biol*., **26**, 445–452.
66. Gurley,L.R., D'Anna,J.A., Barham,S.S., Deaven,L.L. and Tobey,R.A. (1978) Histone phosphorylation and chromatin structure during mitosis in chinese hamster cells. *Eur. J. Biochem.*, **84**, 1–15.
67. Routh,A., Sandin,S., Rhodes,D., A.,R., S.,S. and D.,R. (2008) Nucleosome repeat length and linker histone stoichiometry determine chromatin fiber structure. *Proc. Natl. Acad. Sci. U.S.A.*, **105**, 8872–8877.
68. Song,F., Chen,P., Sun,D., Wang,M., Dong,L., Liang,D., Xu,R.M., Zhu,P. and Li,G. (2014) Cryo-EM study of the chromatin fiber reveals a double helix twisted by tetranucleosomal units. *Science*, **344**, 376–380.
69. Happel,N., Doenecke,D., N.,H. and D.,D. (2009) Histone H1 and its isoforms: contribution to chromatin structure and function. *Gene*, **431**, 1–12.
70. Clausell,J., Happel,N., Hale,T.K., Doenecke,D. and Beato,M. (2009) Histone H1 subtypes differentially modulate chromatin condensation without preventing ATP-Dependent remodeling by SWI/SNF or NURF. *PLoS One*, **4**, e0007243.
71. Oberg,C., Izzo,A., Schneider,R., Wrange,O. and Belikov,S. (2012) Linker histone subtypes differ in their effect on nucleosomal spacing in vivo. *J. Mol. Biol.*, **419**, 183–197.
72. Collepardo-Guevara,R., Portella,G., Vendruscolo,M., Frenkel,D., Schlick,T. and Orozco,M. (2015) Chromatin unfolding by epigenetic modifications explained by dramatic impairment of internucleosome interactions: a multiscale computational study. *J. Am. Chem. Soc.*, **137**, 10205–10215.
73. Ridsdale,J.A., Hendzel,M.J., Delcuve,G.P. and Davie,J.R. (1990) Histone acetylation alters the capacity of the H1 histones to condense transcriptionally active/competent chromatin. *J. Biol. Chem.*, **265**, 5150–5156.
74. Kostova,N.N., Srebreva,L., Markov,D.V., Sarg,B., Lindner,H.H. and Rundquist,I. (2013) Histone H5-chromatin interactions in situ are strongly modulated by H5 C-terminal phosphorylation. *Cytom. Part A*, **83**, 273–279.
75. Talasz,H., Helliger,W., Puschendorf,B. and Lindner,H. (1996) In vivo phosphorylation of histone H1 variants during the cell cycle. *Biochemistry*, **35**, 1761–1767.
76. Zheng,Y., John,S., Pesavento,J.J., Schultz-Norton,J.R., Schiltz,R.L., Baek,S., Nardulli,A.M., Hager,G.L., Kelleher,N.L. and Mizzen,C.A. (2010) Histone H1 phosphorylation is associated with transcription by RNA polymerases I and II. *J. Cell Biol.*, **189**, 407–415.